# ASYMMETRIC JET IMPINGEMENT ON A ROTATING SURFACE

**Corey Klinkhamer**
Department of Mechanical Engineering
University of Windsor
401 Sunset Ave,
N9B 3P4, Windsor, Ontario, Canada
klinkha@uwindsor.ca

**Jerry Adjetey**
Department of Mechanical Engineering
University of Windsor
401 Sunset Ave,
N9B 3P4, Windsor, Ontario, Canada
adjeteyj@uwindsor.ca

**Ram Balachandar**
Department of Mechanical Engineering
University of Windsor
401 Sunset Ave,
N9B 3P4, Windsor, Ontario, Canada
rambala@uwindsor.ca

## ABSTRACT

In this work, a turbulent jet impinging asymmetrically on a rotating surface is numerically investigated using the Reynolds Stress Transport model. Turbulence characteristics of the flow field are analyzed for a jet Reynolds number of $1.3\times10^3$ and a rotational Reynolds number of $175\times10^3$. The nozzle-to-impingement surface distance is five times the diameter ($d$) and the diameter of the impingement surface is $12d$. Experimental results from literature are used to validate the mean circumferential velocity and circumferential Reynolds stress predictions. Circumferential velocity contours in various axial planes aided in the identification of jet and rotation-dominated regimes, where the jet-dominated regime is characterized by axisymmetric jet expansion about the jet axis. A mixing zone, where the wall jet collides with the swirling flow induced by rotation, was also observed and appears as a region of enhanced turbulence. By observing the circumferential turbulence intensities, a bending of the jet before impingement was also noted. A region of shearing between the wall jet region and swirling flow is reported and exists particularly when the jet Reynolds number is low and the rotational Reynolds number is high. As shown in this study, the rotation of the impingement surface leads to intricate mean flow and turbulence characteristics that can potentially influence and enhance heat transfer rates for cooling applications.

## INTRODUCTION

Liquid jet impingement has been used in many industry applications that require high heat and mass transfer rates. More recently, jets have been employed for the thermal management of electric motors, where the jet fluid impinges directly on the rotor which undergoes fixed axis rotation. The flow field induced in rotor cooling applications is highly turbulent and complex, hence it is useful to analyze how impinging jets behave when the impingement surface is rotating. In literature, jets impinging on stationary surfaces have been studied in detail. Various parameters such as jet Reynolds number, jet-to-impingement surface distance, and nozzle type have been investigated. However, jets impinging on rotating surfaces have been far less studied.

A schematic of a jet impinging on a rotating surface is shown in Figure 1a. Firstly, the jet fluid is issued from a circular nozzle of diameter $d$ and then impinges on the rotating impingement surface, of radius $R$, located at a distance $l$ from the nozzle exit. It is widely accepted that a jet-to-impingement surface distance of $l = 5d$ is optimal for heat transfer applications when the impingement surface is stationary (Gardon and Akfirat, 1965), hence in this study, the stand-off distance is maintained at $l/d = 5$. The flow field can be described in cylindrical coordinates, where the origin of the cylindrical coordinate system is located at the center of the impingement surface. The radial $r$-axis is defined as positive outwards from the origin and the axial $z$-axis is defined as positive upwards from the impingement surface. The circumferential direction $\theta$ is positive as determined by the right-hand rule. The mean velocity field can be described by the mean radial $V_r$, mean circumferential $V_\theta$ and mean axial $V_z$ velocity components, illustrated at an arbitrary radial location in Figure 1a. In this work, the jet nozzle axis is offset a distance of $r_{imp}$ from the axis of rotation, therefore the jet is considered to impinge asymmetrically on the rotating surface. Furthermore, in Figure 1b, key flow features in an unrolled $\theta$-$z$ plane are shown along the impingement radius. Two wall jets are formed and are defined as the upstream wall jet and the downstream wall jet. Further in the upstream ($-\theta$) direction exists a swirling flow, which is induced by rotation. In scenarios where the rotation flow dominates the jet flow, a collision between the swirling flow and the upstream wall jet will occur which causes enhanced mixing and turbulence.

Several researchers have first studied the mean flow field and turbulence characteristics of a jet impinging axisymmetrically on a rotating surface. Minagawa and Obi (2004) used laser Doppler anemometry (LDA) to study the influence of rotation on the turbulence characteristics associated with a jet impinging on a rotating surface. At higher rotational Reynolds numbers, a stretching and acceleration of the wall jet was reported which has the potential to improve convective heat transfer rates as demonstrated by Manceau et al. (2014). Other studies investigated the effects of jet-to-impingement surface distance, jet Reynolds number, rotational Reynolds number, and nozzle-to-impingement surface radius ratio (Nguyen et al., 2012; Poncet et al., 2013; Jiang et al., 2021). Nguyen et al., (2012) used particle image velocimetry (PIV) to measure the mean flow and turbulence

quantities of a confined air jet impinging on a rotating surface at a small stand-off distance ($l/d$ = 0.25). Keeping the jet Reynolds number constant and varying the rotational Reynolds number from $0.33\times10^5$ to $5.32\times10^5$, they reported a recirculation zone near the jet centerline that causes an enhanced entrainment effect which is not noticed for jets impinging on stationary surfaces. Moreover, near the periphery of the impingement surface, the flow traveled in the radial direction at low rotational Reynolds numbers but became completely circumferential at higher rotational Reynolds numbers.

Few contributions exist in the literature where the jet nozzle axis is offset relative to the axis of rotation as shown in Figure 1. Metzger et al. (1977) and Brodersen et al. (1996) are the only few studies that analyze a flow field where the axis of the nozzle is offset from the axis of rotation. Both works were experimental contributions that focused on defining jet and rotation-dominated flow regimes. Brodersen et al. (1996) proposed a Reynolds number ratio, $\alpha = Re_j/Re_\omega$, to classify the flow field as rotation-dominated or jet-dominated.

To analyze flow features, particularly near the impingement surface (< 1$d$), several researchers have relied on numerical methods (Manceau et al., 2014; Poncet et al., 2013). Fluid flow prediction for impinging jet flows is a challenging turbulence modeling task, especially when the impingement surface is rotating (Tohidi et al., 2017). High-fidelity simulations were carried out by Oguic et al. (2013) where a Direct Numerical Simulation of an axisymmetric jet

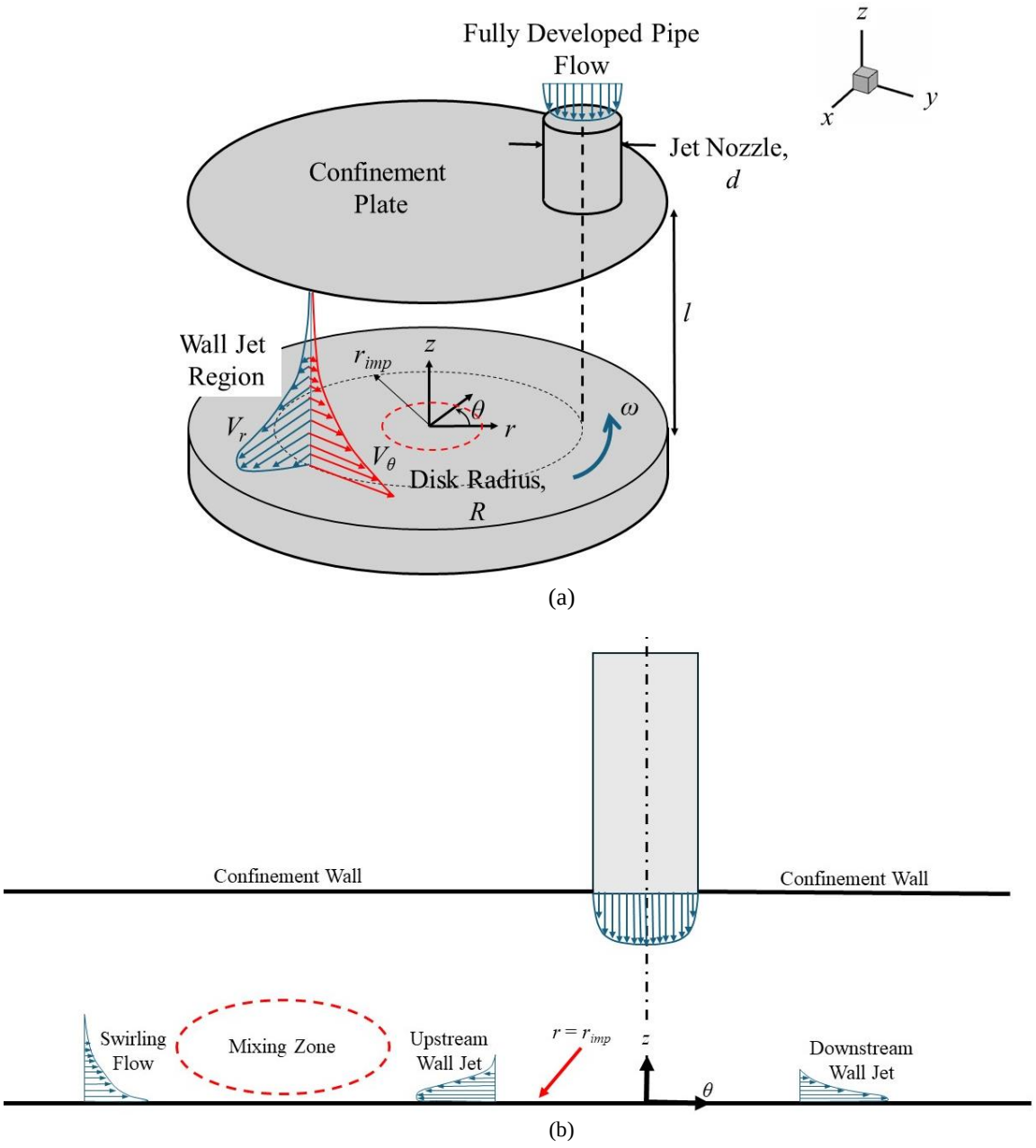


Figure 1. Schematic of (a) a submerged jet impinging on a rotating surface asymmetrically and (b) flow features along the impingement radius $r_{imp}$ in an "unrolled" $\theta$-$z$ plane.

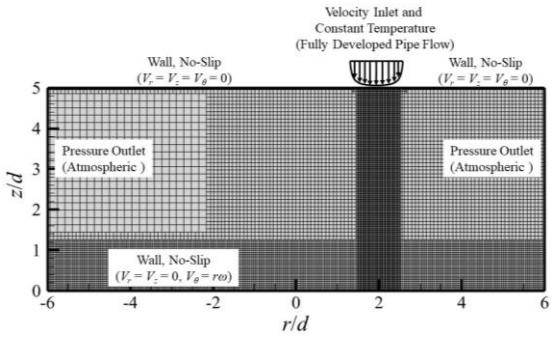


Figure 2. Domain and mesh used to carry out the computations. Boundary conditions are highlighted.

impinging on a rotating surface was studied. To reduce computational costs and to study higher Reynolds number effects, a Reynold Stress Transport Model is often employed along with elliptic blending (EB-RSM). The choice of this turbulence model when comparing mean flow and turbulence quantities was arrived at by Manceau et al. (2014). When comparing the flow characteristics with the experimental results of Minagawa and Obi (2004), Manceau et al. (2014) found that EB-RSM provided the best match with experimental measurements in comparison to other RANS turbulence models. Similar conclusions have been drawn by other researchers (Poncet et al., 2013).

Given the existing literature, there are limited studies investigating submerged liquid jets impinging on rotating surfaces asymmetrically. Moreover, there are no numerical contributions studying jets impinging asymmetrically on rotating surfaces. This paper provides a numerical contribution where the mean flow field and turbulence characteristics of a liquid jet impinging on a rotating surface asymmetrically are studied numerically using an EB-RSM turbulence model.

## METHODOLOGY

Key parameters of interest, and their influence on the mean flow and turbulence characteristics, are considered in this work. The parameters of focus in this study are the jet Reynolds number and rotational Reynolds number which are defined, respectively, as

$$Re_j = \rho U_j d/\mu \quad (1)$$

$$Re_\omega = \rho R^2 \omega/\mu. \quad (2)$$

In Equations 1 and 2, $U_j$ is the bulk jet velocity, $\omega$ is the rotational speed of the impingement surface, $d$ is the nozzle diameter and $R$ is the impingement surface radius. The variables $\mu$ and $\rho$ are the dynamic viscosity and density of the working fluid, water, and are evaluated at room temperature. Moreover, the radius of impingement, jet-to-impingement surface distance, and impingement surface diameter are $R$/3, 5$d$, 12$d$, respectively. In this work, an unsteady Reynolds-Averaged Navier-Stokes (RANS) modeling approach is implemented where the timestep is $1.5\times10^{-4}$ seconds. The conservation of mass and momentum equations, after Reynolds decomposition are

$$\frac{\partial \rho}{\partial t} + \nabla \cdot (\rho \bar{\boldsymbol{v}}) = 0 \quad (3)$$

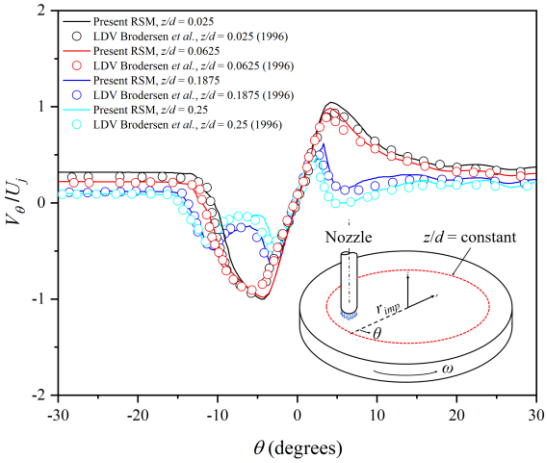


Figure 3. Validation of the circumferential velocity non-dimensionalized by the bulk jet velocity ($V_\theta/U_j$) predicted from the present EB-RSM

$$\frac{\partial}{\partial t}(\rho \bar{\boldsymbol{v}}) + \nabla \cdot (\rho \bar{\boldsymbol{v}} \otimes \bar{\boldsymbol{v}}) = -\nabla \cdot \bar{p}\boldsymbol{I} + \nabla \cdot (\boldsymbol{T} + \boldsymbol{T_t}) + \boldsymbol{f_b}, \quad (4)$$

where $\boldsymbol{v}$, $p$, $\rho$, $\boldsymbol{I}$, and $\boldsymbol{T_t}$, represent the velocity vector, pressure, density, identity tensor, and Reynolds stress tensor, respectively. It should be noted that vectors are indicated with a bold typeface and mean quantities are identified with an overbar. The body force $\boldsymbol{f_b}$, appears in Equation 4To model the Reynolds stress tensor, a Reynolds Stress Transport turbulence model is used with elliptic blending, which introduces six transport equations used to solve each Reynolds stress component. Further details of elliptic blending can be found in literature (Manceau and Hanjalic, 2002).

The computational domain is shown in a meridian plane in Figure 2. For discretizing the domain, a hexahedral mesh topology is chosen with around 8 million cells used over the entire domain. The mesh was refined within the shear layer of the jet and near the impingement surface where there will be large velocity gradients. At the inlet, a fully developed velocity profile is applied. Atmospheric pressure is assigned at the domain outlet. At the impingement surface, a no-slip boundary condition is applied where $V_r = V_z = 0$ and $V_\theta = r\times\omega$. A no-slip boundary condition is also applied at the upper confinement wall where $V_r = V_z = V_\theta = 0$.

## MODEL VALIDATION

Validation of the numerical model was first carried out through mean circumferential velocity comparisons with the experimental results of Brodersen et al. (1996) and is shown in Figure 3. For this validation case only, the jet and rotational Reynolds numbers were $5.17\times10^4$ and $5.09\times10^5$, respectively with a jet-to-impingement surface distance of 1.5$d$. In Figure 3, the mean circumferential velocity distributions from $-30° \leq \theta \leq 30°$ in the $r$-$\theta$ plane located in the range $0.025 \leq z/d \leq 0.25$ are compared. As indicated, there is a good match between the numerical and experimental predictions with a maximum error of about 2%. Further validation of the turbulence characteristics was carried out through a comparison with the LDA measurements of Minagawa and Obi (2004). In this validation case, the jet and rotational Reynolds numbers were $1.45 \times 10^4$ and $2.45 \times 10^5$, respectively with a jet-to-impingement surface distance of 5$d$. In Figure 4, the Reynolds

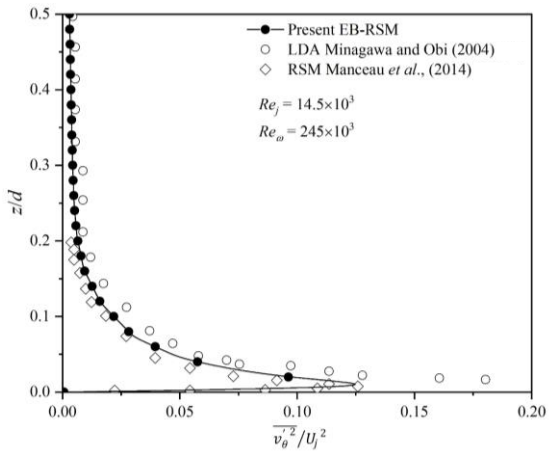


Figure 4. Validation of the of the circumferential Reynolds stress component predicted from the present EB-RSM

stresses in the circumferential direction at a radial location of $r = 5d$ are shown over the axial range of $z/d = 0$ to 0.5. Generally, a good agreement between the present EB-RSM and LDA measurements can be seen, however there is a notable mismatch in the peaks near the impingement surface. It should be noted that Minagawa and Obi (2004) reported around 20% uncertainty in the measured peaks of the Reynolds stresses near the wall. Furthermore, under identical conditions, the circumferential Reynolds stress predictions from the present EB-RSM are compared with the RSM predictions of Manceau et al. (2014) with good agreement over the entire spatial range. Hence the present numerical model is deemed to be reliable.

## RESULTS

When a jet impinges on a stationary surface, the axial and radial velocity components are dominant. However, when the impingement surface rotates, a circumferential velocity component is introduced which can often be the dominant velocity component. As the circumferential velocity component appears to be the most influenced by rotation, it is critical to analyze this velocity component. In Figure 5, contours of the mean circumferential velocity non-dimensionalized by the bulk jet velocity ($V_\theta/U_j$) are shown in two axial planes, $z/d = 0.012$ and $z/d = 0.125$. Streamtraces are also superimposed onto each contour to illustrate the behavior of the jet upon impingement. Like previous researchers, jet and rotation-dominated regions are identified. A parameter is introduced and is referred to as the radius of axisymmetric jet expansion $r_{exp}$. The radius of axisymmetric jet expansion is measured relative to the nozzle axis and extends up to a point where the streamtraces become deflected into the direction of rotation. In Figure 5, the region of axisymmetric jet expansion is highlighted by the green circle. At a location near the impingement surface ($z/d = 0.012$) it appears that the jet cannot penetrate the swirling flow induced by the rotating impingement surface. A "film", defined as the region of swirling flow into which the jet cannot penetrate, is formed on the rotating surface. Consequently, in this region, the radial velocity component is near zero and the velocity vectors point completely in the circumferential direction. As indicated by the streamtraces, the jet cannot fully penetrate the film, and the region of axisymmetric jet expansion does not exist (i.e. $r_{exp} = 0$). It should also be noted that the maximum circumferential velocity in the wall jet region is nearly five times less than that at the periphery of the impingement surface at $z/d = 0.012$, which indicates the strong dominance of the rotating impingement surface in this region of the flow field. Further from the impingement surface at $z/d = 0.125$, the effects of rotation are still prominent as shown by significant deflection of the wall jet and streamtraces in the counter-clockwise direction, however, the region of axisymmetric jet expansion exists and is approximately equal to $2d$. Since the jet does not penetrate the swirling flow and hence does not impinge onto the rotating surface when $Re_j = 1.3\times10^3$ and $Re_\omega = 175 \times 10^3$, the flow field can be considered rotation-dominated.

In Figure 6, distributions of the mean circumferential velocity non-dimensionalized by the bulk jet velocity ($V_\theta/U_j$) are shown over the angular displacement range $-60° \leq \theta \leq 60°$ along the impingement radius. The distributions are shown in various axial planes ($z/d$ = constant). When the flow

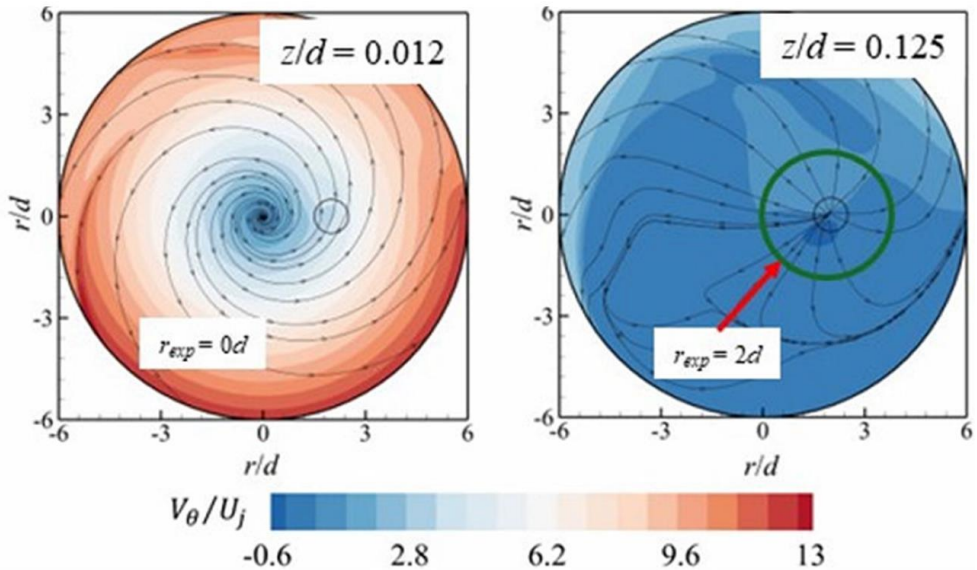


Figure 5. Contours of circumferential velocity non-dimensionalized by the bulk jet velocity ($V_\theta/U_j$). Contours are shown in two axial planes defined as $z/d = 0.012$ and 0.125.

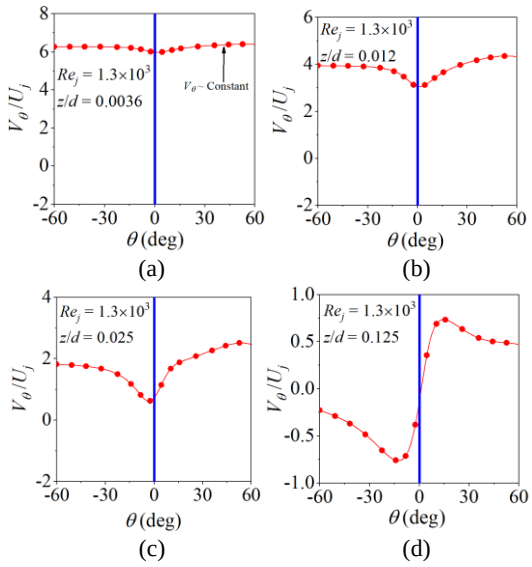


Figure 6. Distributions of circumferential velocity non-dimensionalized by the bulk jet velocity ($V_\theta/U_j$). Distributions are shown at (a) $z/d$ = 0.0036, (b) $z/d$ = 0.012, (c) $z/d$ = 0.025 and (d) $z/d$ = 0.125.

field is completely rotation-dominated (i.e. $Re_\omega$ is high, $Re_j$ is low or jet does not exist), the mean circumferential velocity component will be approximately constant over the entire range of angular displacement as an axisymmetric swirling flow is formed. This is demonstrated in Figure 6a where the swirling flow is shown to be dominant near the impingement surface ($z/d$ = 0.0036) which is indicated by a near uniform distribution of $V_\theta$ over the entire range of angular displacement. It is expected that as the jet penetrates the swirling flow, the circumferential momentum of the swirling flow is transferred into the axial and radial directions which leads to lower circumferential velocities at the jet axis ($\theta = 0°$). However, since the flow field is strongly rotation-dominated at $z/d$ = 0.0036, the jet does not completely penetrate the

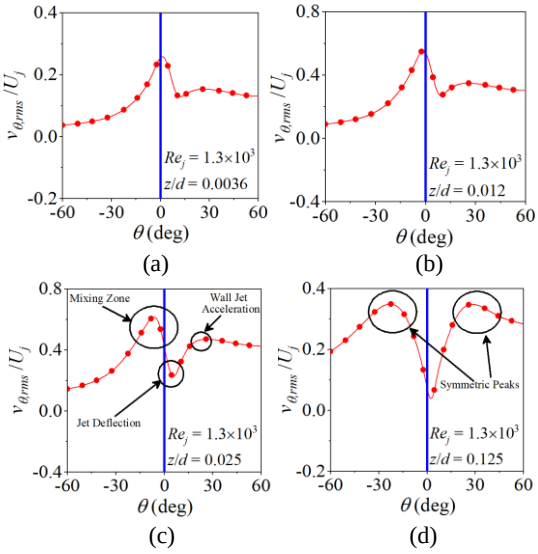


Figure 7. Distributions of circumferential turbulence intensity non-dimensionalized by the bulk jet velocity ($v_{\theta,rms}/U_j$). Distributions are shown at (a) $z/d$ = 0.0036, (b) $z/d$ = 0.012, (c) $z/d$ = 0.025 and (d) $z/d$ = 0.125.

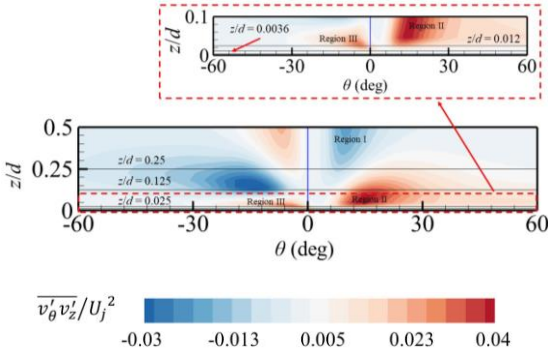


Figure 8. Contour of the Reynolds shear stress component in a $\theta$-z plane non-dimensionalized by the bulk jet velocity square ($\overline{v_\theta' v_z'}/U_j^2$) located at $r = r_{imp} = R/3$

swirling flow, therefore the circumferential velocity never approaches zero at the jet axis (indicated by the blue line). As the effects of rotation become weaker away from the impingement surface such as at $z/d$ = 0.012, the jet better penetrates the swirling flow and there is a greater transfer of momentum from the circumferential direction to the radial and axial directions which corresponds to lower circumferential velocities near the jet axis. At $z/d$ = 0.125 (Figure 6d), the jet dominates the flow field indicated by the negative circumferential velocity which means the jet expands against the direction of rotation.

In Figure 7, distributions of the turbulence intensity in the circumferential direction non-dimensionalized by the bulk jet velocity ($v_{\theta,rms}/U_j$) are shown over the angular displacement range -60° ≤ $\theta$ ≤ 60° in various axial planes. When a jet impinges on a stationary surface, two symmetric peaks in the $v_{\theta,rms}$ distributions are present about the jet axis. As suggested in Figure 7, the peaks are no longer symmetric about the jet axis. One peak exists in the upstream direction towards the swirling flow (-$\theta$ direction) which can be linked to the mixing of the wall jet and swirling flow in the mixing zone as shown in Figure 7c. A local minimum is present in the same horizontal planes and is located in the downstream direction away from the swirling flow (+$\theta$ direction). The local minimum coincides with the jet centerline which gets deflected into the direction of rotation when the jet Reynolds number is low and the rotational Reynolds number is high, therefore the local minimum is offset from the nozzle centerline (shown by the blue line). A secondary peak is formed when the downstream wall jet accelerates radially outward. In horizontal planes further from the impingement surface ($z/d \geq 0.125$), the peak in the mixing zone diminishes as the swirling flow becomes weak which indicates there is less mixing. Moreover, the local minimum and hence jet centerline experiences less deflection in axial planes sufficiently far from the impingement surface.

It is beneficial to study the non-dimensionalized Reynolds shear stress ($\overline{v_\theta' v_z'}/U_j^2$) in the $\theta$-z plane as it impacts mixing within the flow field. Three regions of high shear stresses, shown in Figure 8, are evident in the flow field, and these regions are summarized as follows. Region I is characterized by the shearing between the free jet and stagnant ambient fluid. In Region I the stagnant ambient fluid is entrained by the jet which aids in the expansion of the jet. Region II is developed by the shearing between the wall jet and ambient fluid. Regions I and II exhibit traits much like jets impinging on stationary surfaces and are antisymmetric about the nozzle

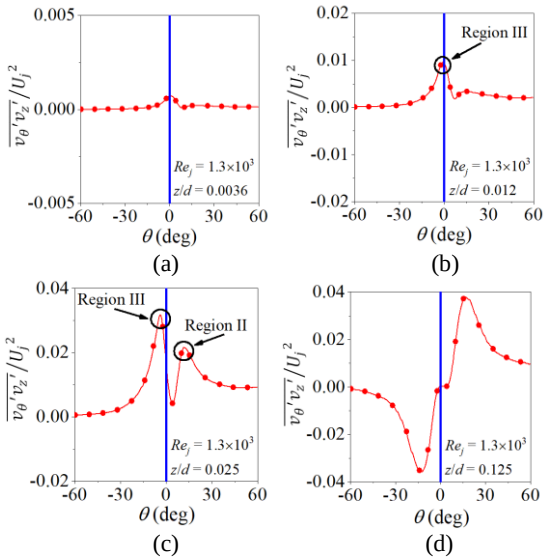


Figure 9. Distributions of the Reynolds shear stress component in a $\theta$-$z$ plane non-dimensionalized by the bulk jet velocity square ($\overline{v_\theta' v_z'}/U_j^2$) located at $r = r_{imp} = R/3$. Distributions are shown at (a) $z/d$ = 0.0036, (b) $z/d$ = 0.012, (c) $z/d$ = 0.025 and (d) $z/d$ = 0.125.

axis if the flow field is jet-dominated. An additional Region III is formed which can be attributed to the shearing between the upstream wall jet and swirling flow. When the jet Reynolds number is low at $Re_j = 1.3\times10^3$ and the rotational Reynolds number is high at $Re_\omega = 175\times10^3$, Region III will be well defined. However, for high jet Reynolds numbers and low rotational Reynolds numbers, it is expected that Region III will diminish due to less shearing between the upstream wall jet and swirling flow as the flow field becomes jet-dominated. Another important observation is that the presence of Region III causes Region II to become inclined in the upstream direction (-$\theta$ direction).

Distributions of $\overline{v_\theta' v_z'}/{U_j}^2$ at $r = r_{imp} = R/3$ over the angular displacement range -60° ≤ $\theta$ ≤ 60° are shown in Figure 9 in various axial planes. At $z/d$ = 0.0036, there is little shearing between the wall jet and swirling flow as shown by negligible values of $\overline{v_\theta' v_z'}$ in Figure 9a. It should be noted that $z/d$ = 0.0036 is very near to the impingement surface and is located below Region III (see Figure 8). At $z/d$ = 0.012 the effects of shearing between the swirling flow and upstream wall jet (in Region III) begin to be notable as shown by a peak of positive magnitude located slightly in the upstream direction (-$\theta$ direction) from the nozzle axis which is indicated in Figure 9b. Further from the impingement surface at $z/d$ = 0.025, two positive peak values of the shear stress are located on either side of the jet axis (Figure 9c). The peak in the -$\theta$ direction is due to shearing in Region III whereas the peak in the +$\theta$ direction is due to shearing in Region II. The antisymmetry of the profile in Figure 9d is a result of the shearing between the developing wall jet and the ambient fluid.

## CONCLUSIONS

A jet impinging on a rotating surface was studied numerically using an EB-RSM turbulence model. Numerical model predictions were validated using experimental measurements from the literature. Circumferential velocity contours in various axial planes aided in the identification of jet and rotation-dominated regimes, where the jet-dominated regime is characterized as a region of axisymmetric jet expansion about the jet axis. A mixing zone, where the wall jet and swirling flow induced by rotation collide, was created and is associated with enhanced circumferential turbulence intensities. A shift in the location of the local minimum of the circumferential turbulence intensity distribution indicates the bending of the jet prior to impingement. Finally, three regions of dominant shearing were identified: Region I defined as shearing between the free jet region and stagnant ambient fluid, Region II defined as shearing between the wall jet region and stagnant ambient fluid, and Region III defined as shearing between the wall jet and swirling flow.

## REFERENCES

Brodersen, S., Metzger, D. E., and Fernando, H. J. S., 1996, "Flows Generated by the Impingement of a Jet on a Rotating Surface: Part I—Basic Flow Patterns", *Journal of Fluids Engineering*, *118*(1), 61–67. https://doi.org/10.1115/1.2817514

Gardon, R., and Akfirat, J. C., 1965, "The role of turbulence in determining the heat-transfer characteristics of impinging jets", *International Journal of Heat and Mass Transfer*, *8*(10), 1261–1272. https://doi.org/10.1016/0017-9310(65)90054-2

Jiang, L., Lyu, Y., Zhu, P., Gao, W., and Liu, Z., "Numerical Investigation of Conjugate Heat Transfer on a Rotating Disk Under Round Liquid Jet Impingement", *International Journal of Thermal Sciences*, Vol. 170, 2021.

Manceau, R., and Hanjalic, K., "Elliptic Blending Model: A New Near-Wall Reynolds-Stress Turbulence Closure", *Physics of Fluids*, Vol. 14, 2002, pp. 744

Manceau, R., Perrin, R., Hadžiabdić, M., and Benhamadouche, S., 2014, "Investigation of the interaction of a turbulent impinging jet and a heated, rotating disk", *Physics of Fluids*, *26*(3), 035102. https://doi.org/10.1063/1.4867380

Metzger, D. E., and Grochowsky, L. D., "Heat Transfer Between an Impinging Jet and a Rotating Disk", *Journal of Heat Transfer*, 99(4), pp. 663–667, (1977).

Minagawa, Y., and Obi, S., 2004, "Development of turbulent impinging jet on a rotating disk", *International Journal of Heat and Fluid Flow*, *25*(5), 759–766. https://doi.org/10.1016/j.ijheatfluidflow.2004.05.013

Nguyen, N., Pellé, J., Harmand, J. S., and Poncet, S., "PIV measurements of an air jet impinging on an open rotor-stator system", *Exp. Fluids*, Vol. 53, 2012 pp. 401–412

Oguic, R., Poncet, S., and Viazzo, S., "High-order direct numerical simulations of a turbulent round impinging jet onto a rotating heated disk in a highly confined cavity", *International Journal of Heat and Fluid Flow*, Vol. 61, 2016, pp. 366-378

Poncet, S., et al., 2013, "Turbulent Impinging Jet Flow into an Unshrouded Rotor–Stator System: Hydrodynamics and Heat Transfer", *International Journal of Heat and Fluid Flow*, Vol. 44, 2013, pp. 719– 734

Sardasht, M. T., Hosseini, R., and Amani, E., "An analysis of turbulence models for prediction of forced convection of air stream impingement on rotating disks at different angles", *International Journal of Thermal Sciences*, Vol. 118, 2017, pp. 139-151